Direct observation of the displacement field and microcracking in a glass by means of X-ray tomography during in situ Vickers indentation experiment

Tanguy Lacondemine, Julien Réthoré, E Maire, Fabrice Célarié, Patrick Houizot, Clément Roux-Langlois, Christian M Schlepütz, Tanguy Rouxel

Direct observation of the displacement field and microcracking in a glass by means of X-ray tomography during in situ Vickers indentation experiment

Tanguy Lacondemine, Julien Réthoré, Éric Maire, Fabrice Célarié, Patrick Houizot, Clément Roux-Langlois, Christian Schlepütz, Tanguy Rouxel

Full length article

Direct observation of the displacement field and microcracking in a glass by means of X-ray tomography during in situ Vickers indentation experiment

Tanguy Lacondemine [a], Julien Réthoré [b], Éric Maire [c], Fabrice Célarié [a], Patrick Houizot [a], Clément Roux-Langlois [a], Christian M. Schlepütz [d], Tanguy Rouxel [a, *]

[a] Département Mécanique et Verre, IPR, UMR UR1-CNRS 6251, Université de Rennes 1, Campus de Beaulieu, 35042, Rennes Cedex, France
[b] GeM, Ecole Centrale de Nantes, UMR CNRS 6183, Université de Nantes, 1 Rue de La Noë, 44321, Nantes Cedex 3, France
[c] MATEIS, INSA Lyon, UMR CNRS 5510, 7 Avenue de La Capelle, 69621, Villeurbanne Cedex, France
[d] Swiss Light Source, Paul Scherrer Institute, 5232, Villigen PSI, Switzerland

ARTICLE INFO

Article history:
Received 4 June 2019
Accepted 27 July 2019
Available online 30 July 2019

Keywords:
Glass
Indentation
Constitutive behavior
Microcracking
Tomography

ABSTRACT

The actual displacement field in a glass during an in-situ Vickers indentation experiment was determined by means of X-ray tomography, thanks to the addition of 4 vol % of X-ray absorbing particles, which acted as a speckle to further proceed through digital volume correlation. This displacement was found to agree well with the occurrence of densification beneath the contact area. The intensity of the densification contribution (Blister field proposed by Yoffe) was characterized and provides evidence for the significant contribution of densification to the mechanical fields. Densification accounts for 27% of the volume of the imprint for the studied glass, that is expected to be less sensitive to densification than amorphous silica or window glass. A major consequence is that indentation cracking methods for the evaluation of the fracture toughness, when they are based on volume conservation, as in the case of Hill-Eshelby plastic inclusion theory, are not suitable to glass. The onset for the formation of the subsurface lateral crack was also detected. The corresponding stress is ≈ 14 GPa and is in agreement with the intrinsic glass strength.

1. Introduction

Damage caused by sharp contact loading at the surface of a glass is a major scientific and industrial issue. However, despite numerous studies, the mechanics and physics of the indentation deformation and cracking process in brittle materials still raise fundamental questions. For instance, glasses exhibit densification due to their free volume content, so that the mechanical behavior is not simply elasto-plastic (where "plasticity" refers to an isochoric shear constitutive law). Densification accounts for over 80% of the volume of the imprint in the case of vitreous silica and silica-rich glasses [1]. Consequently, both the kinematics and the dynamics of indentation remain inaccurately assessed [2-5]. Nevertheless, a relatively successful description of the problem was found by considering the displacement and stress fields as resulting from the combination of a point-contact field [6] and a so-called "Blister" field, where the latter accounts for a permanent deformation beneath the indenter [7,8]. This permanent deformation arises from densification, thanks to the free volume content of the glass, and from the isochoric shear flow, which is chiefly responsible for the pile-up of matter at the border of the imprint [8]. In this study, a glass matrix particulate composite was synthesized, using strontium aluminate ($SrAl_2O_4$) particles. Interest in such particles is three-fold: i) strontium is an alkaline earth element with a relatively large atomic number ($z = 38$) so that particles provide an excellent contrast with the glassy matrix and can be used as a marker to investigate the displacement field using X-ray tomography, ii) doped with Eu and Dy, $SrAl_2O_4$ (the monoclinic phase) is a mechanoluminescent compound [9], and finally iii) particles are expected to induce some strengthening and toughening effects.

The glass matrix particulate composite was characterized by means of ultrasonic echography and Vickers indentation. The indentation site topography was analyzed by Atomic Force Microscopy (AFM) before and after annealing at the glass transition

* Corresponding author.
E-mail address: tanguy.rouxel@univ-rennes1.fr (T. Rouxel).

temperature (T_g) to evaluate the contribution of densification and shear flow to the permanent imprint formation, following a classical experimental protocol [10-13].

X-ray tomography is a remarkable technique to get insight into the mechanical behavior during a loading cycle by means of in-situ experimental set-ups, and it was successfully applied to brittle materials, and especially ceramics [14-16].

In this study, a specific indentation loading machine [17] was used to perform the mechanical loading in-situ in an X-ray synchrotron for tomographic microscopy. The formation and propagation of the microcracks at the indentation site in a glass could thus be followed live, and the displacement field was also assessed thanks to a Digital Volume Correlation routine (DVC), taking advantage of the particles, which act as a natural speckle. Hence, the 3D displacement field was experimentally measured and could be compared to available analytical solutions.

2. Materials and experimental techniques

2.1. The glass particulate composite

The studied glass matrix particulate composite [$NaPoLi + SrAl_2O_4$] with composition (1-x)($0.25Na_2O - 0.50\ P_2O_5 - 0.25\ Li_2O$), x($SrAl_2O_4$:Eu, Dy), with x = 0.043 was synthesized by the melt-quenching method, as reported by Dubernet *et Al.* [18]). NaH_2PO_4 (Aldrich, 99%), LiH_2PO_4 (Aldrich, 99%), and $SrAl_2O_4$:Eu, Dy (Aldrich, 99%) powders were mixed in a platinum crucible and were prefired at 320 °C for 3 h to remove water from the powder mixture. Then, the crucible was placed for 2 min into a furnace preheated at 800 °C. The glass was then poured into a stainless-steel mold, which was preheated at 250 °C, corresponding to the glass transition temperature of the glassy matrix and further annealed at this temperature for 2 h to reduce the residual stresses. A bimodal particle size distribution was obtained, where the large particles (Ø ≈ 40 μm) aim at reinforcing the material and provide the mechanoluminescent property whereas the smaller ones (Ø ≈ 5 μm) were homogeneously dispersed and showed up as a remarkable natural speckle for DVC. The particles have a much larger X-ray attenuation than the matrix and were thus easily imaged by tomography. The indented surfaces of the sample were polished down to 1 μm with a diamond suspension. The glass matrix being slightly hydrophilic, the material was kept in a desiccator, and the surface was washed with acetone prior to testing.

2.2. Experimental techniques

2.2.1. Elastic properties

The moduli of elasticity of the composite, E (Young) and μ (shear), where measured by ultrasonic echography using 10 MHz piezoelectric transducers and the Poisson's ratio (ν) was further deduced. The reduced modulus ($E_r = E/(1\text{-}\nu^2)$) and hardness (H) of the composite were measured by instrumented Vickers micro-indentation (Fisher H100 XYP) at 100 mN with a 5 mN s^{-1} loading-unloading rate and a dwell time of 5 s.

2.2.2. Indentation behavior

The indentation process involves reversible and irreversible deformation components. The quantity of matter which flowed downward and gave birth to the residual stresses can be estimated from the imprint left once unloading is completed after the densification and isochoric shear flow contribution are deduced (see Ref. [12] for details).

The elastic component can be estimated from the elastic recovery accompanying the unloading stage. The relationship between the recovered depth u_r and the total penetration depth u_t at the maximum load is given by Ref. [19] (Fig. 1):

$$\left(\frac{u_r}{u_t}\right)^2 = 1 - 2\left(1-\nu^2\right)\frac{H}{E}\tan\Psi \tag{1}$$

where Ψ is the apical angle of the axisymmetrical indenter.

The equivalent cone for a Vickers indent (i.e. the cone that would produce a circular imprint of radius a of the same projected area and depth for a given load F as for the Vickers indent) corresponds to $\Psi = 73.5°$.

The geometrical relationship between the indentation volume V_{ig}^- where there is contact between the indenter and the glass and the residual indentation volume V_i^- is given by (Fig. 1):

$$V_i^- = \gamma V_{ig}^- \frac{u_r}{u_t} \tag{2}$$

where $V_{ig}^- = \frac{\pi a^3}{3\tan\Psi}$ with $a = \sqrt{\frac{F}{\pi H}}$ and H the material hardness, and $\gamma = u_t/u_g$ with u_g defined as being the depth of the indenter actually in contact with the glass (Fig. 1).

Thus, replacing u_r/u_t in Eq. (2) by Eq. (1) gives

$$\gamma = \frac{V_i^-}{V_{ig}^-\sqrt{1-2\left(1-\nu^2\right)\frac{H}{E}\tan\Psi}} \tag{3}$$

The best fit to data extracted from the displacement recovery depth on mainly ceramic materials in Ref. [19] yields a value of 0.91 for γ. Using volume recovery data obtained on glasses with different composition, the best agreement was obtained with γ = 0.59 [4].

The indentation volume (permanent imprint) fractions attributed to densification and shear, namely V_R and V_P respectively, were estimated using AFM (Bruker, Nanoscope V, Santa Barbara, CA). The indentation volume that remained once the densified and piled-up volumes were deduced and correlated with the intensity of the residual stress field responsible for microcracking, so that

$$\xi = 1 - V_R - V_P \tag{4}$$

with $V_R = \frac{(V_i^- - V_a^-) + (V_a^+ - V_i^+)}{V_i^-}$ and $V_P = \frac{V_i^+ - (V_a^+ - V_i^+)}{V_i^-}$ (Fig. 1) can be considered as driving force parameters for the indentation cracking process.

The preliminary assessment of the indentation deformation behavior (V_R, V_P and ξ) was conducted by combining indentation experiments and AFM investigations.

Indentation was performed by means of an instrumented micro-indenter (Fisher H100 XYP) with a 5 mN s^{-1} loading and unloading rate up to 100 mN and a 5 s dwell time. Each imprint was then imaged by AFM before and after annealing treatment at 250 °C for 30 min (heating rate: 10° min^{-1}, cooling rate: 2° $min.^{-1}$). Indentation and pile-up volumes were estimated from AFM images using the "find holes" and "find hills" tools of WSxM [20] software (Fig. 2).

2.2.3. Synchrotron X-ray tomography in-situ indentation

The in situ indentation experiments were performed at the TOMCAT beamline [21] of the Swiss Light Source in Villigen (Switzerland). A 30 keV monochromatic parallel X-ray beam was used and the lateral size of the voxels was set to 0.325 μm by the optics of the camera. Series of 1500 projections (radiographs) were recorded every 0.12-degree (for an overall rotation of 180-degree) at the rate of 200 ms per projection, on a Charge Couple Device

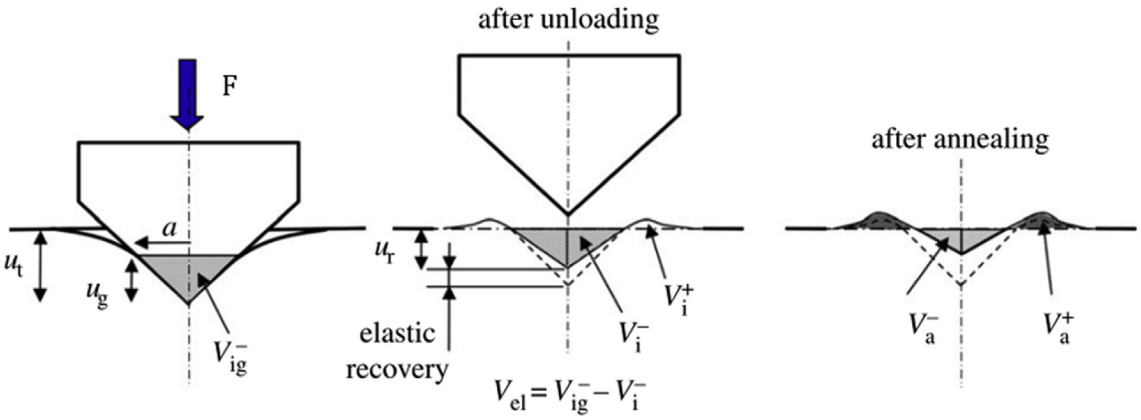

Fig. 1. Schematic drawing of the volume topological analysis by means of AFM [2].

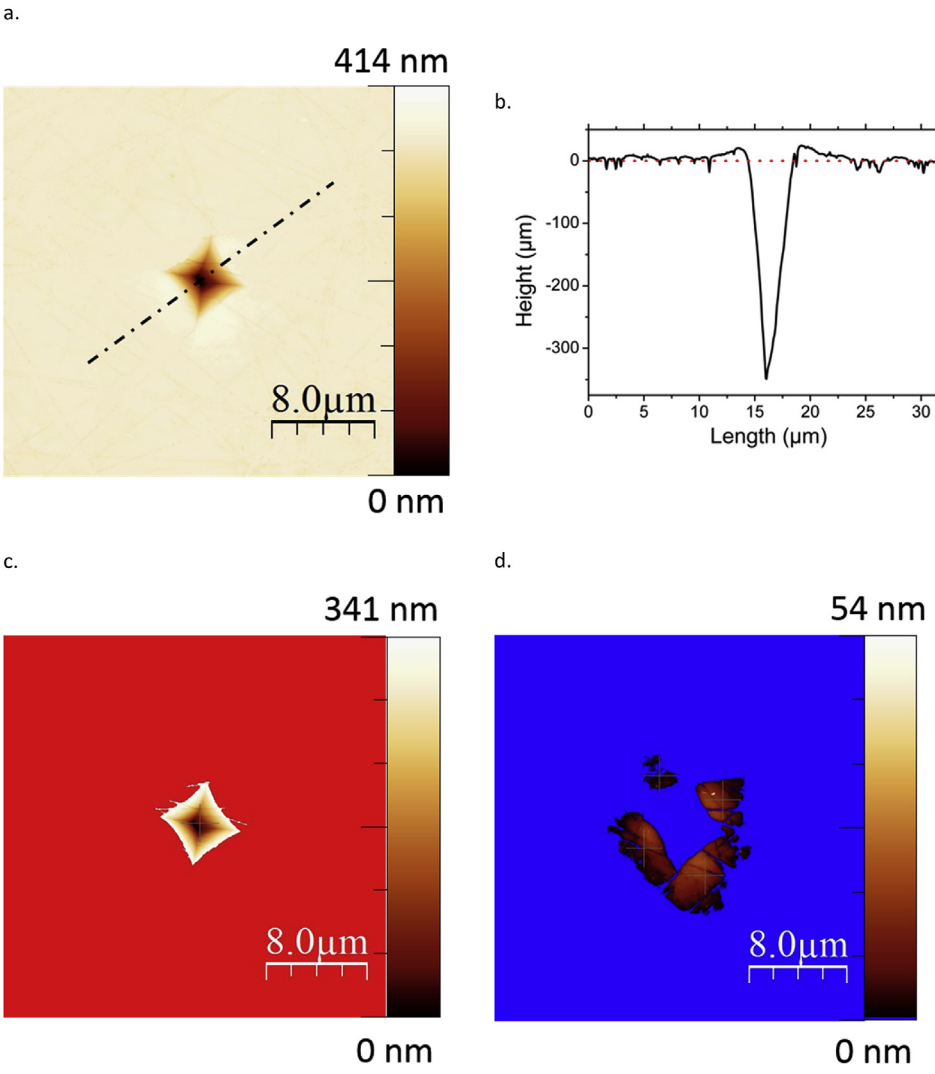

Fig. 2. Indentation imprint topography: a.) AFM image (tapping); b.) profile across the center, normal to the edges; c.) indentation volume (1.981 μm^3); and d.) pile-up volume (0.328 μm^3).

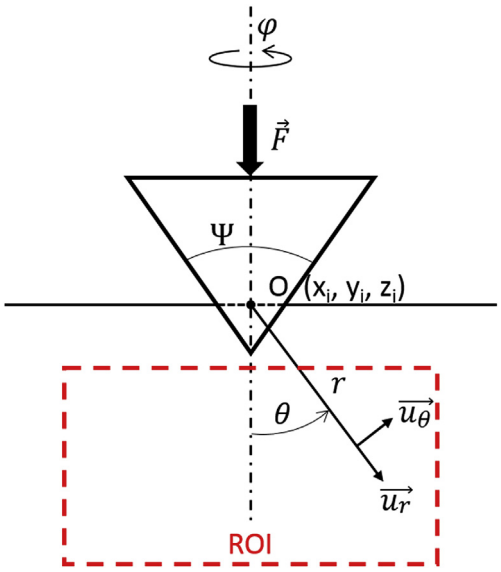

Fig. 3. Indentation coordinates and Region Of Interest (ROI) used for the Digital Volume Correlation (DVC) protocol.

(CCD) pco.edge™ camera with array of 2560 × 2160 pixels. The radiographic projections were reconstructed into 8-bit grey scale 3D images (2560 × 2560 x 2160 pixels), with artifacts correction.

Samples were produced by fiber drawing from a 10 mm diameter preform (preform speed $v_p = 2\ m\ min^{-1}$, drawing speed $v_d = 0.02\ m\ min^{-1}$, drawing temperature $T_d = 390\ °C$) to obtain cylinders, 3 mm in diameter [22]. A complete loading-unloading cycle was applied to the samples, from 0 to 30 N by steps of 5 N, with a loading-unloading speed of $0.3\ \mu m\ s^{-1}$. The load was maintained constant during the image recording lasting for 5 min at each load step.

The specific machine used for this experiment was designed to perform high speed X-ray tomography during in situ experiment [17]. The rotating connector and the fine balance of this set up inhibit unwanted movements during rotation and thus inadvertent offsets between two consecutive scans.

2.3. Numerical methods

2.3.1. Digital volume correlation

Digital Volume Correlation combined with X-ray tomography of sample with microstructural detail is a well-known technique for displacement field measurement by subvolume tracking [23]. The DVC analysis was carried out, using the UFreckles software [24,27], with 16 finite elements over a selected volume (Region Of Interest "ROI", cf. Fig. 3) of 1276 × 1276 x 1248 pixels located beneath the indentation site. A median filter taking into account the first neighbors of each node was applied to reduce the noise.

The DVC provided the displacement field (U_x, U_y, U_z) in cartesian coordinates inside the ROI for different loads both during loading and unloading stages.

2.3.2. Comparison between the experimental and analytical displacement field

The displacement field in an elastic material experiencing densification (at stress typically larger than 1 GPa in the case of glasses; i.e. near the sharp contact loading area) submitted to an indentation test is obtained by superposing the Boussinesq's stress field [6] (elastic part) and a field stemming from a strain nucleus built on three force dipoles, referred to as the "Blister" field and accounting for the densified region [7]. The blister is only an approximate expression (based on the doublet force problem analyzed by Love [28]) for the densification responsible for microcracking. However, a good agreement was reached between the experimental displacement field, obtained by DVC, and the one described by considering the blister field (see § 3.2.3 and Fig. 9). In spherical coordinates, the displacement vector is expressed as (Fig. 3):

$$\boldsymbol{u_r}(\boldsymbol{r},\boldsymbol{\theta}) = \frac{\boldsymbol{F}}{4\pi\mu\boldsymbol{r}}[\boldsymbol{4(1-4\nu)\cos\theta - (1-2\nu)}] + \frac{\boldsymbol{B}}{\mu\boldsymbol{r}^2}\left[\boldsymbol{2(1-\nu) - (5-4\nu)\cos^2\theta}\right] \tag{5}$$

$$\boldsymbol{u_\theta}(\boldsymbol{r},\boldsymbol{\theta}) = \frac{\boldsymbol{F}}{4\pi\mu\boldsymbol{r}}\left[\frac{\boldsymbol{(1-\nu)\sin\theta}}{\boldsymbol{1+\cos\theta}} - \boldsymbol{(3-4\nu)\sin\theta}\right] + \frac{\boldsymbol{B}}{\mu\boldsymbol{r}^2}\boldsymbol{2(1-2\nu)\sin\theta\cos\theta} \tag{6}$$

with $B = V_i^- \xi \frac{3E}{4\pi(1+\nu)(1-2\nu)}$ [11] and $V_i^- = \gamma V_{ig}^- \sqrt{1-2(1-\nu^2)\frac{H}{E}\tan\Psi}$ from Eq. (3).

Aiming at optimizing the parameters of the analytical expression to best fit the experimental data, B is the sole adjustable material parameter. However, to access the actual displacement field ($\vec{u}$), the indentation site coordinates (the loading axis x_i, y_i and the surface z_i locations) and the rigid body motion (translations X, Y, Z and rotations R_X, R_Y, R_Z) must be determined first. In order to achieve this goal, the indentation site location (coordinates x_i, y_i, z_i, as estimated from the reference tomographic image before loading for F = 1 N at the intersection of the indenter loading axis and the sample surface) was defined as the origin of the cartesian system ($x(i) = x_0(i) - x_i$, $y(j) = y_0(j) - y_i$ and $z(k) = z_0(k) - z_i$, where x(i),y(j),z(k) became the new coordinate of each point $x_0(i)$,$y_0(j)$,$z_0(k)$ of the ROI). Then, the rigid body motion (X, Y, Z and R_X, R_Y, R_Z), resulting from the displacement of the specimen during loading, were added to the analytical displacement field. Because of its strong influence on the optimization convergence, the position of the loading axis (x_i, y_i) was hence adjusted. Lastly, the surface location (z_i) and the Blister magnitude (B) were tuned to best fit the experimental data and the analytical expression and the numerical value of B was further compared with the theoretical one.

Because of the large strain and displacement induced in the vicinity of the contact area, the optimization is limited to points located further than 2a from the origin ($r \geq 2a$), where the analytical displacement field is defined (Eqs. (5) and (6)). To minimize the difference between the experimental displacement field and the theoretical one, namely U and u(P) with P = [B, x_i, y_i, z_i, X, Y, Z, R_X, R_Y, R_Z], an iterative least square minimization algorithm expressed as in the following Eqs. (7) and (8) was used.

$$\min_{dP} \boldsymbol{U} - \boldsymbol{u}(\boldsymbol{P}+\boldsymbol{dP})^2 \Leftrightarrow \min_{dP} \boldsymbol{U} - \left(\boldsymbol{u}(\boldsymbol{P}) + \frac{\boldsymbol{du}(\boldsymbol{P})}{\boldsymbol{dP}}\boldsymbol{dP}\right)^2 \tag{7}$$

$$\Leftrightarrow \begin{bmatrix} dP_1 \\ \vdots \\ dP_m \end{bmatrix} = \left(\begin{bmatrix} \frac{\partial u(P)_1}{\partial P_1} & \cdots & \frac{\partial u(P)_1}{\partial P_m} \\ \vdots & \ddots & \vdots \\ \frac{\partial u(P)_n}{\partial P_1} & \cdots & \frac{\partial u(P)_n}{\partial P_m} \end{bmatrix}^T \begin{bmatrix} \frac{\partial u(P)_1}{\partial P_1} & \cdots & \frac{\partial u(P)_1}{\partial P_m} \\ \vdots & \ddots & \vdots \\ \frac{\partial u(P)_n}{\partial P_1} & \cdots & \frac{\partial u(P)_n}{\partial P_m} \end{bmatrix} \right)^{-1} \begin{bmatrix} \frac{\partial u(P)_1}{\partial P_1} & \cdots & \frac{\partial u(P)_1}{\partial P_m} \\ \vdots & \ddots & \vdots \\ \frac{\partial u(P)_n}{\partial P_1} & \cdots & \frac{\partial u(P)_n}{\partial P_m} \end{bmatrix}^T \left(\begin{bmatrix} U_1 \\ \vdots \\ U_n \end{bmatrix} - \begin{bmatrix} u(P)_1 \\ \vdots \\ u(P)_n \end{bmatrix} \right) \tag{8}$$

With n: number of nodes x 3 (displacement components: x, y and z) and m: number of parameters.

Moreover, some (limited) additional shear may be induced by the geometrical imperfection of the specimen (angle between upper and lower surfaces) and by the occurrence of some device misalignment. This additional shear must be considered prior to optimization by adding a term to u_x and u_y depending linearly on z (i.e. $u_x = u_x + kz$, with k constant).

3. Results and discussion

3.1. Indentation behavior

The indentation parameters were determined by applying a 100 mN load. This load was high enough to affect a volume larger than the elementary representative volume (imprint volume 7–8 μm^3, imprint diagonal 6–7 μm, particle size ~40 μm and measured first neighbor distance ~60 μm). At the same time, it was small enough to avoid the formation of visible cracks and to allow for the imaging of the imprint by AFM in a "reasonable" time (15 min).

The measured indentation volumes (V_i^-, V_i^+, V_a^-, V_a^+) yield calculated values for γ and ξ of 0.35 and 0.57 respectively (Table 1) (Young's modulus E and hardness (H) of the composite material (homogenized value) were used). Note that the volume affected by the indentation during the in-situ experiments ($V_{ig}^- = 4.10^4$ μm^3 and a = 47 μm at F = 30 N vs $V_{ig}^- = 7.55$ μm^3 and a = 1.45 μm at F = 100 mN) was much larger than the one associated with the determination of γ and ξ so that the composite properties (Table 2) were relevant to the analysis of the in-situ experiments.

3.2. In-situ tomography experiments

3.2.1. Indentation crack formation

Indentation induces stresses on loading as large as hardness, e.g. in the GPa range. This stress field is sufficiently intense to initiate radial/median cracks (driven by the $\sigma_{\phi\phi}$ stress component Eq. (9)) from pre-existing flaws or from the edges of the imprint, which act as singularities. Permanent deformation occurs concomitantly upon loading and its densification and pile-up components yield some relaxation of the residual stress field, while the remaining isochoric flow is responsible for a non-zero value of B (B is proportional to 1-V_R-V_P). In order to visualize the crack shape in 3D and to "remove" the particles, a simple thresholding was not efficient. Hence, a median projection on the z (loading axis) direction was used. Indeed, the cracks are large, straight and visibile over numerous consecutive slices whereas the particles are small and dispersed. The projection chosen to eliminate the particles (small ones) was performed over 50 slices, with a two slice step in order to reduce the computational time. An additional treatment based on the object circularity analysis enabled to dissociate the cracks from the remaining particles (Fig. 4).

The analytical form of the stress field associated with the displacement field (Eqs. (5) and (6)) is expressed as:

$$\sigma_{\phi\phi}(r,\theta) = \frac{(1-2\nu)F}{2\pi r^2}\left[\cos\theta - \frac{1}{1+\cos\theta}\right] + \frac{2B}{r^3}(1-2\nu)\left(2-3\cos^2\theta\right) \tag{9}$$

$$\sigma_{\theta\theta}(r,\theta) = \frac{F}{2\pi r^2}\frac{(1-2\nu)\cos^2\theta}{1+\cos\theta} - \frac{2B}{r^3}(1-2\nu)\cos^2\theta \tag{10}$$

$$\sigma_{rr}(r,\theta) = \frac{F}{2\pi r^2}[1-2\nu-2(2-\nu)\cos\theta] + \frac{4B}{r^3}\left[(5-\nu)\cos^2\theta - 2 + \nu\right] \tag{11}$$

where F is the contact load (N). Due to the axisymmetrical loading case, the stress components $\sigma_{r\phi}(r,\theta)$ and $\sigma_{\theta\phi}(r,\theta)$ are nil. The expression of the $\sigma_{r\theta}(r,\theta)$ component is not given here because $\sigma_{r\theta}$ is not discussed in the present analysis (its expression can be found in Ref. [4]).

During unloading, the elastic recovery tends to reduce the

Table 1
Measured indentation volumes and calculated indentation parameters.

F (mN)	a (μm)	V_{ig}^- (μm^3)	V_i^-(μm^3)	V_a^-(μm^3)	V_i^+(μm^3)	V_a^+(μm^3)	γ	ξ
100	2.72	7.55	2.05±0.09	1.45±0.16	0.26±0.06	0.26±0.09	0.35±0.01	0.58±0.06

Table 2
Materials properties.

	ρ (g.cm^{-3})	E (GPa)	ν	H (GPa)	E_r (GPa)
NaPoLi [18]	2.24 ± 0.01	53±1	0.29 ± 0.002	3.7 ± 0.36	54 ± 0.92
$SrAl_2O_4$ [29,30]	3.5	102	0.23	6.8	
Composite (3% Vol.)	2.52 ± 0.01	55 ± 1.2	0.27 ± 0.005	4.2 ± 0.03	62.4 ± 0.6

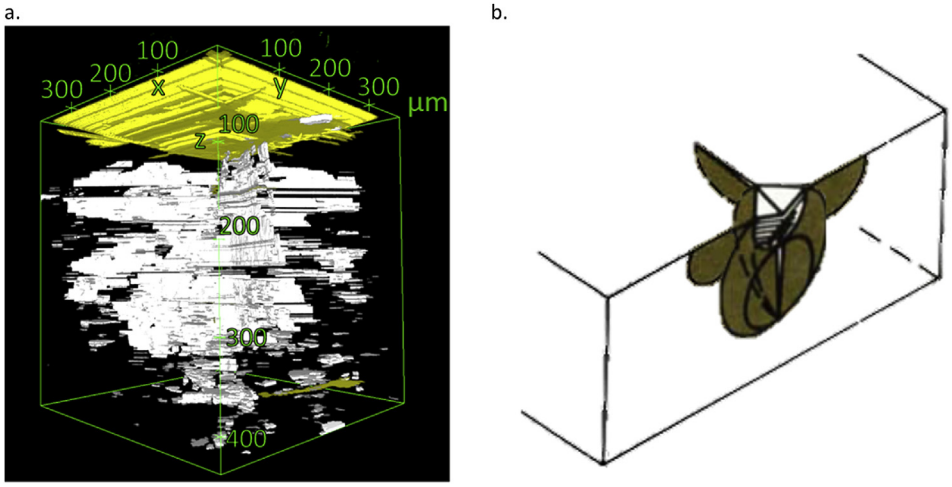

Fig. 4. Radial-median cracks: a.) 3D visualization, in light grey, at maximum load (F = 30 N); and b.) idealized morphology (Cook and Pharr [5]).

volume of the imprint (as the depth diminishes), while the densified volume opposes the eslastic springback. Eqs (9) and (10) provide a mathematical description of this phenomenon. As F is deacreased, the Boussinesq's field weakens while the Blister field remains constant, resulting in residual stresses which increase upon unloading (especially $\sigma_{rr}(\theta = 0)$); eventually generating new cracks (such as the subsurface lateral ones responsible for the formation of chips at indentation sites). In-situ indentation experiments enable to determine the critical stress inducing subsurface crack formation by following simultaneously the stress change during unloading and the onset for crack formation on tomographic images. For NaPOLi glass with $SrAl_2O_4$ particles, with a maximum load $F_{max} = 30$ N, subsurface lateral cracks that are driven by $\sigma_{rr}(\theta = 0)$ (Eq. (11)) show upon unloading for a stress value between 13 and 14 GPa (Fig. 5).

3.2.2. DVC: displacement field and discontinuities

The displacement field under the indenter could be obtained with a remarkable resolution thanks to the finely dispersed ceramic particles. Some displacement discontinuities were identified (correlation error), which stem from the occurrence of microcracks. The loading situation being axisymmetrical, U_x and U_y are expected to exhibit clear changes across any (Oz) containing plane. The U_x displacement and the correlation error are investigated over half of the ROI, cut by the (Oxz) plan (Fig. 6a and b). Ux displacement profiles are then extracted from the (Oxz) plan to follow the evolution of the transversal displacement with respect to the loading axis (Fig. 6 c). Due to the Vickers indenter geometry and the presence of cracks, the same results can be obtained in the (Oyz) plan.

After removing the rigid body motion, the displacement magnitude due to the indentation does not exceed 6.3 voxels or 2.05 µm (Fig. 6 a) and is symmetrical with respect to the indenter axis (Fig. 6 c). The jump of displacement under the indent is too smooth to provide information about crack presence and crack opening. To this extent, the correlation error provides additional information regarding crack location, shape and length (Fig. 6 b).

3.2.3. Confrontation of the experimental displacement field to the analytical one – determination of the blister magnitude

As a preliminary remark, it is noteworthy that transposing the analysis discussed in § III.1 and stemming from experiments at 100 mN to indentation experiments performed at loads as large as 30 N raises serious questions. In particular, the indentation size effect (ISE) [31], tip radius effect (concerning the Vickers diamond tip as well as the AFM probe tip) and the occurrence of cracking may have some incidence on the measured indentation volumes and thus on the value of γ (Table 1). In addition, the presence of cracks is not accounted for in the analytical model. As this is discussed below, this is a source of error when comparing the analytical and the experimental displacement fields.

The analytical expression of the displacement field (u_x, u_y, u_z) is compared to the experimental one (U_x, U_y, U_z) and parameter B (Eqs. (5) and (6)) is adjusted to minimize the discrepancy.

The obtained value for B is then compared to the analytical one. A good agreement was found upon loading with less than 9% error: $B_{analytic} = 13.8 \times 10^{-5}$ N m vs $B_{exp} = 12.5 \times 10^{-5}$ N m for the third experiment at $F_{max} = 30$ N. Although the analytical value for B remains constant upon unloading, the adjusted value decreases until it reaches only 70% of the expected value: $B_{exp} = 9.6 \times 10^{-5}$ N m for F = 2.5 N (Fig. 7). It is hypothesized that the presence of cracks reduces the apparent stiffness of the material and thus enhance the elastic spring back effect, further resulting in a decrease of B.

Nevertheless, the gap between the experimental and the analytical (fitted) displacement fields, as quantified by analyzing the minimization residue U-u, does reaches 0.85 µm (~40% of the experimental displacement (Fig. 8)).

The analysis of the displacement along the x axis reveals that the Boussinesq's contribution (Fig. 8 a) is effective over a larger distance than the Blister field, which incidence is limited to the vicinity of the indentation area and the masked region (Fig. 8 b). Moreover, a comparison between the experimental displacement field U_x (Fig. 8 c) and the residue U_x-u_x (Fig. 8 d), clearly shows that the displacement due to the Blister field along the x axis coincides

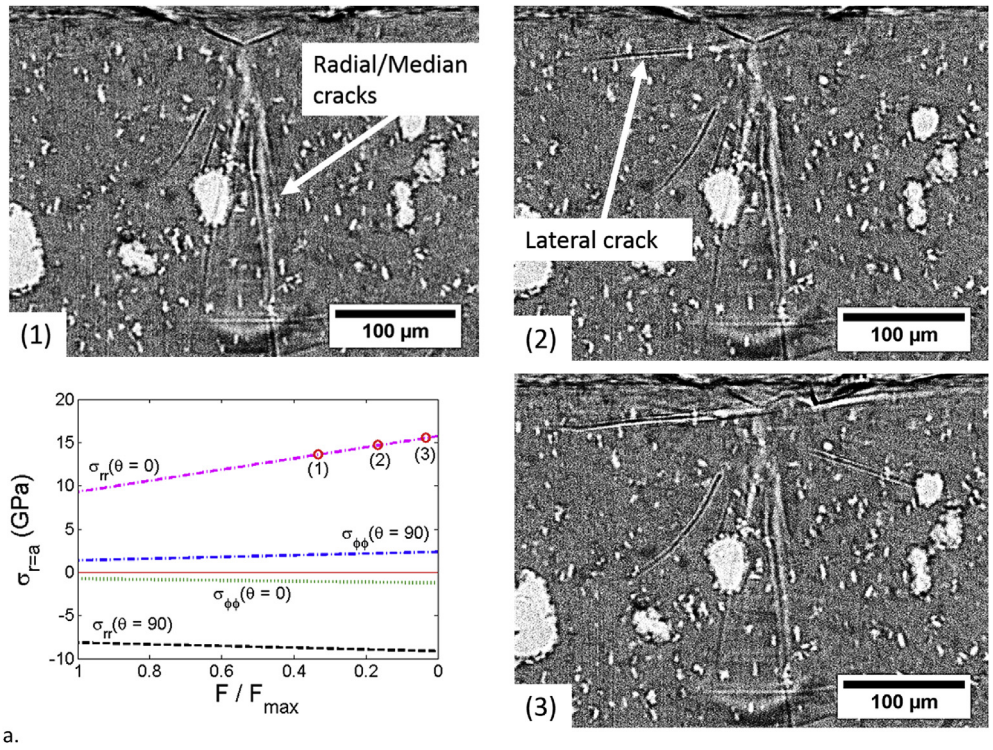

Fig. 5. a.) Evolution of the indentation stress components during unloading together with the in-situ tomographic images of the lateral crack formation and propagation at loads of (1) F = 10 N, (2) F = 5 N and (3) F = 1 N.

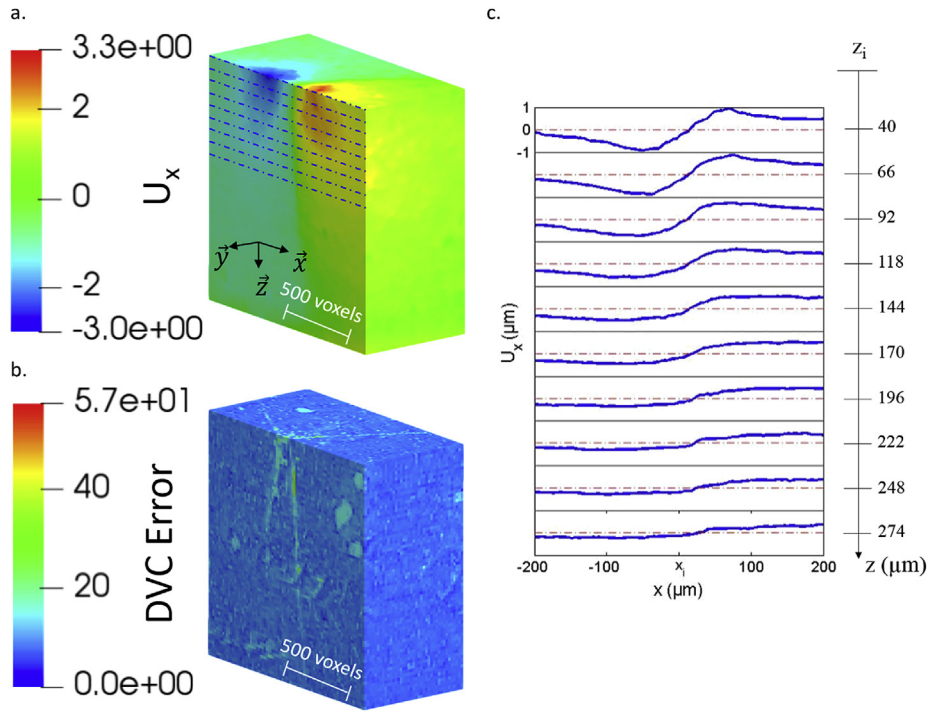

Fig. 6. Displacement along the x axis (a.) and correlation error (b.) in voxel (1 voxel = 0.325 µm) over half of the ROI halved by the plane (y_i, z) and evolution of Ux along the z axis in the plane (y_i, z) in µm (c.) at a maximum load of F_{max} = 30 N.

to the experimental displacement field, with a residue approaching zero near the surface. In a region away from the contact area, where the Boussinesq's contribution prevails, the residual displacement U_x-u_x reaches an absolute value of 2.6 voxels (= 0.845 µm).

Regarding the vertical component of the displacement (Fig. 9) and the corresponding residue U_z-u_z (Fig. 9 d), the identification of the relative influence of the Boussinesq's (Fig. 9 a) and of the Blister (Fig. 9 b) fields is not straightforward. The Boussinesq's component,

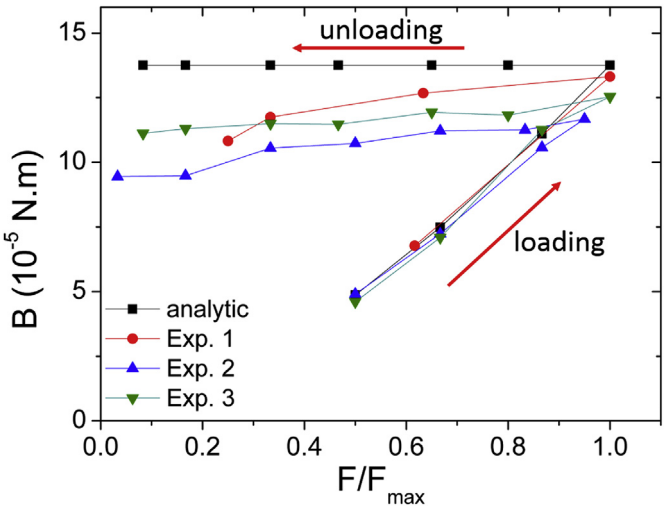

Fig. 7. Evolution of the Blister B in function of the load normalized by the maximum load $F_{max} = 30$ N.

u_z(Boussinesq), and the experimental displacement, U_z (Fig. 9 c), look similar with a residual difference of 1.5 voxels far away from the imprint. This difference is due to a residual displacement in the Boussinesq's far field ($u(r, \Theta) \propto 1/r$). It is only in a small region located under the masked area, where the Blister is the most significant, that a positive residue of 1.4 voxels, at most, is obtained.

As it was said earlier, the large displacement and the decrease of the specimen stiffness that are induced by the occurrence of microcracks make the confrontation of the theory (limited to the deformation process) to the experiment difficult. For instance, the residual strain ε_{xx}(U-u) (Fig. 10 a) (and ε_{yy}(U-u) by symmetry), is small (ε_{xx}(U-u) = 0 ± 0.005), but when microcracks form ε_{xx}(U-u) > 0.01. The residual displacement magnitude (max(U_x-u_x) - min(U_x-u_x) = 4.1 pixels = 1.33 μm) along the x direction is therefore stemming from the presence of microcracks and corresponds to the maximum radial/median crack opening. Likewise, the strain ε_{zz}(U-u) (Fig. 10 b) is extremely small over most of the ROI, ε_{zz}(U-u) = 0 ± 0.005, but for a small volume under the masked region, where ε_{zz}(U-u) < −0.01.

In spite of the various experimental and theoretical problems met on the way to compare experimental and analytical fields, the actual displacement field is found in agreement with the one predicted on the basis of a relatively simple approach due to Boussinesq and Yoffe although it was developed for crack-free systems (i.e. for a smaller contact load). Besides, the confrontation provides information about the crack localization and geometry. For example, plotting the contour of ε_{xx}(U-u) + ε_{yy}(U-u) = 0.01 allows to access the crack morphology in 3D (Fig. 10 c), in addition to the 2D traces observed in the tomographic images.

4. Conclusion

The application of X-ray tomography to study the indentation behavior of a glass was found very fruitful. Thanks to digital volume correlation, the full displacement field could be determined, in 3D, during the loading and unloading stages as well. An important result is that the actual displacement field agrees well with the one predicted by the simple Boussinesq-Yoffe analytical model, hence providing evidence for a significant contribution of densification to the mechanical fields. Densification was found experimentally to account for 27% of the volume of the imprint (twice as much as for the shear flow). A major consequence is that indentation cracking methods for the evaluation of the fracture toughness, when they are based on volume conservation, as in the case of Hill-Eshelby plastic inclusion theory, are not suitable to glass. A numerical value for the intensity of the “blister” field governing the densification was obtained ($B \sim 13 \times 10^{-5}$ N m). Besides, some displacement jumps were detected, that allow to trace the formation of

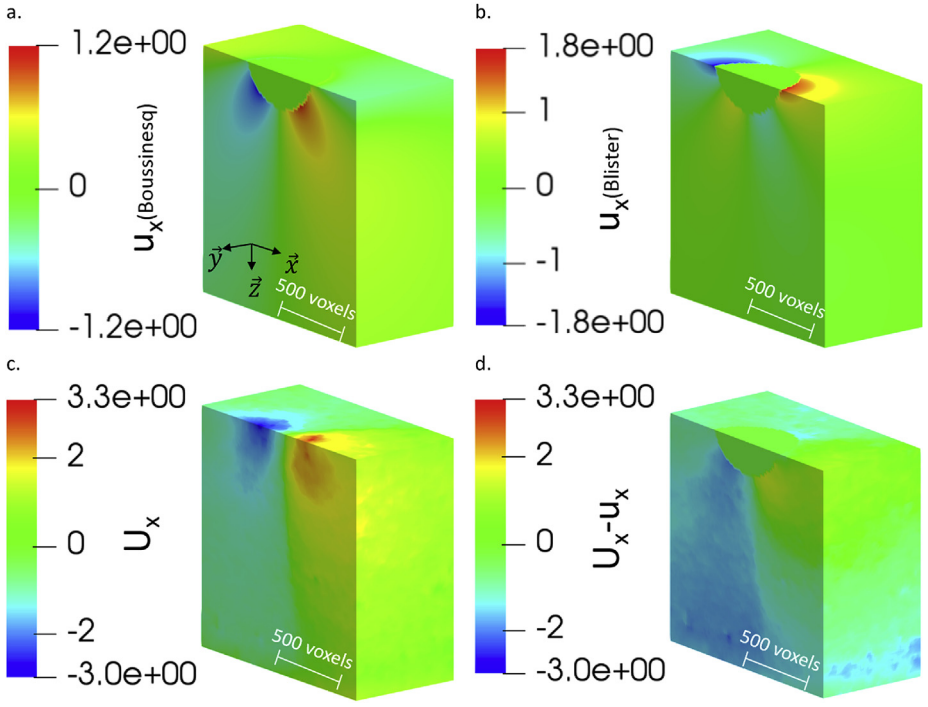

Fig. 8. Displacement fields along the x axis, in voxels, over half the ROI at maximum load ($F_{max} = 30$ N): a.) Boussinesq; and b.) Blister displacement field, as derived from Eqs. (5) and (6); c.) experimental displacement field; and d.) confrontation residue.

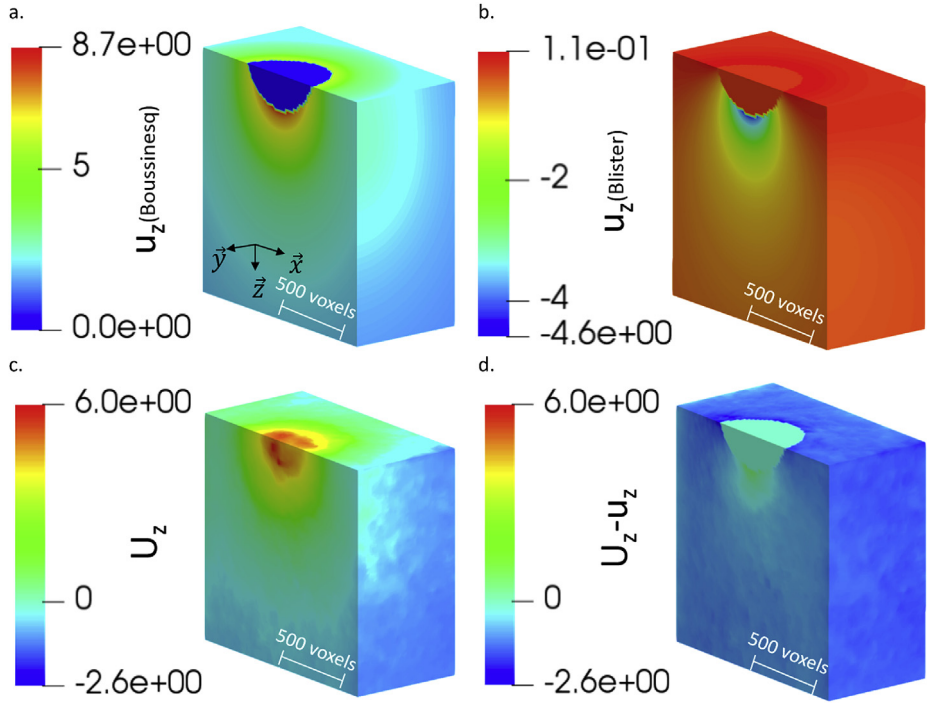

Fig. 9. Displacement fields along the z axis, in voxels, over half the ROI at maximum load ($F_{max} = 30$ N): a.) Boussinesq; and b.) Blister field (analytical); c.) experimental displacement field; and d.) confrontation residue.

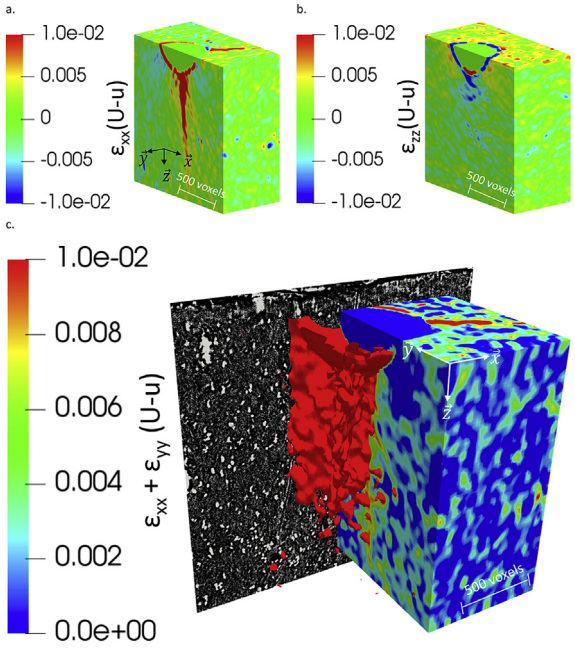

Fig. 10. Strain residues along: a.) x; and b.) z axes; c.) 3D crack visualization (ε_{xx}(U-u) + ε_{yy}(U-u) = 0.01) in association with tomographic slice and ε_{xx} + ε_{yy} residue in voxel at maximum load ($F_{max} = 30$ N).

microcracks at the indentation site. In particular, the formation of a subsurface lateral crack (almost parallel to the surface) beneath the indentation site on unloading was observed, consistently with the theoretical prediction. A major finding is that the stress ($\sigma_{rr}(\theta = 0)$) associated with the onset of this crack is about 14 GPa, that is in good agreement with the intrinsic glass strength or with Orowan's expression for the theoretical strength.

Declaration of interest

None.

Acknowledgements

We acknowledge the Paul Scherrer Institute (Villigen, Switzerland) for provision of synchrotron radiation beamtime at the TOMCAT beamline X02DA of the SLS. The authors are very grateful to Catherine Boussard and Hervé Orain for sample preparation. This work was supported by the European Research Council (ERC Advanced Grant Number 320506).

References

[1] S. Yoshida, J.-C. Sanglebœuf, T. Rouxel, Quantitative evaluation of indentation-induced densification in glass, J. Mater. Res. 20 (12) (2005) 3404–3412.
[2] P. Sellappan, T. Rouxel, F. Celarie, E. Becker, P. Houizot, R. Conradt, Composition dependence of indentation deformation and indentation cracking in glass, Acta Mater. 61 (16) (2013) 5949–5965.
[3] V. Keryvin, L. Charleux, R. Hin, J.P. Guin, J.C. Sangleboeuf, Mechanical behaviour of fully densified silica glass under Vickers indentation, Acta Mater. 129 (2017) 492–499.
[4] T. Rouxel, Driving force for indentation cracking in glass: composition, pressure and temperature dependence, Philos. Trans. Ser. A, Math. Phys. Eng. Sci. 373 (2038) (2015) 20140140.
[5] R.F. Cook, G.M. Pharr, Direct observation and analysis of indentation cracking in glasses and ceramics, J. Am. Ceram. Soc. 73 (4) (1990) 787–817.
[6] J.M. Boussinesq, Application des potentiels à l'étude de l'équilibre et du mouvement des solides élastiques, Gauthier-Villars, Paris, France, 1885, p. 734.
[7] E.H. Yoffe, Elastic stress fields caused by indenting brittle materials, Philos. Mag. A 46 (4) (1982) 617–628.
[8] T. Rouxel, H. Ji, J.P. Guin, F. Augereau, B. Ruffle, Indentation deformation mechanism in glass: densification versus shear flow, J. Appl. Phys. 107 (2010) 094903.
[9] P. Jha, B.P. Chandra, Impulsive excitation of mechanoluminescence in $SrAl_2O_4$: Eu, Dy phosphors prepared by solid state reaction technique in reduction atmosphere, J. Lumin. 143 (2013) 280–287.
[10] S. Yoshida, H. Sawasato, T. Sugawara, Y. Miura, J. Matsuoka, Effects of indenter geometry on indentation-induced densification of soda-lime glass, J. Mater.

Res. 25 (11) (2011) 2203–2211.
[11] K.G. Aakermann, K. Januchta, J.A.L. Pedersen, M.N. Svenson, S.J. Rzoska, M. Bockowski, J.C. Mauro, M. Guerette, L. Huang, M.M. Smedskjaer, Indentation deformation mechanism of isostatically compressed mixed alkali aluminosilicate glasses, J. Non-Cryst. Solids 426 (2015) 175–183.
[12] K. Januchta, R.E. Youngman, A. Goel, M. Bauchy, S.J. Rzoska, M. Bockowski, M.M. Smedskjaer, Structural origin of high crack resistance in sodium aluminoborate glasses, J. Non-Cryst. Solids 460 (2017) 54–65.
[13] G. Scannell, D. Laille, F. Célarié, L. Huang, T. Rouxel, Interaction between Deformation and crack Initiation under Vickers Indentation in Na_2O–TiO_2–SiO_2 glasses, Front. Mater. 4 (6) (2017) 1–10.
[14] M. Mostafavi, N. Baimpas, E. Tarleton, R.C. Atwood, S.A. McDonald, A.M. Korsunsky, T.J. Marrow, Three-dimensional crack observation, quantification and simulation in a quasi-brittle material, Acta Mater. 61 (16) (2013) 6276–6289.
[15] Y. Vertyagina, M. Mostafavi, C. Reinhard, R. Atwood, T.J., Marrow, In situ quantitative three-dimensional characterisation of sub-indentation cracking in polycrystalline alumina, J. Eur. Ceram. Soc. 34 (12) (2014) 3127–3132.
[16] A. Bouterf, J. Adrien, E. Maire, X. Brajer, F. Hild, S. Roux, Identification of the crushing behavior of brittle foam: from indentation to oedometric tests, J. Mech. Phys. Solids 98 (2017) 181–200.
[17] E. Maire, C. Le Bourlot, J. Adrien, A. Mortensen, R. Mokso, 20 Hz X-ray tomography during an in situ tensile test, Int. J. Fract. 200 (1–2) (2016) 3–12.
[18] M. Dubernet, Y. Gueguen, P. Houizot, F. Célarié, J.-C. Sangleboeuf, H. Orain, T. Rouxel, Evidence and modeling of mechanoluminescence in a transparent glass particulate composite, Appl. Phys. Lett. 107 (15) (2015) 151906.
[19] B.R. Lawn, V.R. Howes, Elastic recovery at hardness indentations, J. Mater. Sci. 16 (10) (1981) 2745–2752.
[20] I. Horcas, R. Fernández, J.M. Gomez-Rodriguez, J. Colchero, J. Gómez-Herrero, A. Baró, WSXM: a software for scanning probe microscopy and a tool for nanotechnology, Rev. Sci. Instrum. 78 (1) (2007) 013705.
[21] M. Stampanoni, A. Groso, A. Isenegger, G. Mikuljan, Q. Chen, A. Bertrand, S. Henein, R. Betemps, U. Frommherz, P. Böhler, D. Meister, M. Lange, and R. Abela, Trends in synchrotron-based tomographic imaging: the SLS experience, in SPIE Optics + Photonics. 2006, International Society for Optics and Photonics. p. 63-77.
[22] P. Houizot, F. Smektala, V. Couderc, J. Troles, L. Grossard, Selenide glass single mode optical fiber for nonlinear optics, Opt. Mater. 29 (6) (2007) 651–656.
[23] B.K. Bay, T.S. Smith, D.P. Fyhrie, M. Saad, Digital volume correlation: three-dimensional strain mapping using X-ray tomography, Exp. Mech. 39 (3) (1999) 217–226.
[24] B.K. Bay, Methods and applications of digital volume correlation, J. Strain Anal. Eng. Des. 43 (8) (2008) 745–760.
[27] J. Réthoré, Ufreckles, 2018. Available from: https://doi.org/10.5281/zenodo.1433776.
[28] A.E.H. Love, A Treatise on the Mathematical Theory of Elasticity, Dover Publications Inc, New York, NY, 1927.
[29] M. Dubernet, Mécanoluminescence de composites particulaires à matrice vitreuse, Doctorat Thesis, in: Institut de Physique de Rennes, vol. 1Université de Rennes, 2016, p. 117.
[30] M. Nanko, S. Taniguchi, K. Matsumaru, *Densified Eu2+-doped $SrAl_2O_4$ by pulsed electric current sintering*, Adv. Technol. Mater. Mater. Process. J. 9 (2007) 125–130.
[31] H. Li, R.C. Bradt, The indentation load/size effect and the measurement of the hardness of vitreous silica, J. Non-Cryst. Solids 146 (1992) 197–212.